[0000-0002-6305-3252]
[0000-0002-1365-1908]
[0000-0002-6075-1813]

Draft version April 12, 2022
Typeset using LaTeX **modern** style in AASTeX62



# Radial evolution of thermal and suprathermal electron populations in the slow solar wind from 0.13 to 0.5 au : Parker Solar Probe Observations.

Joel B. Abraham,[1] Christopher J Owen,[1] Daniel Verscharen,[1,2] Mayur Bakrania,[1] David Stansby,[1] Robert T. Wicks,[3] Georgios Nicolaou,[4] Phyllis L Whittlesey,[5] Jeffersson A. Agudelo Rueda,[1] Seong-Yeop Jeong,[1] and Laura Berčič[1]

[1] *Mullard Space Science Laboratory, UCL, Holmbury St. Mary, Dorking, Surrey, RH5 6NT, UK*
[2] *Space Science Center, University of New Hampshire, Durham NH 03824, USA*
[3] *Department of Mathematics, Physics and Electrical Engineering, Northumbria University, Newcastle upon Tyne, NE1 8ST, UK*
[4] *Southwest Research Institute, San Antonio, TX 78238, USA*
[5] *Space Sciences Laboratory, University of California, Berkeley, CA 94720, USA*

(Received -; Revised -; Accepted -)

Submitted to ApJ

## ABSTRACT

We develop and apply a bespoke fitting routine to a large volume of solar wind electron distribution data measured by Parker Solar Probe (PSP) over its first five orbits, covering radial distances from 0.13 to 0.5 au. We characterise the radial evolution of the electron core, halo and strahl populations in the slow solar wind during these orbits. The fractional densities of these three electron populations provide evidence for the growth of the combined suprathermal halo and strahl populations from 0.13 to 0.17 au. Moreover, the growth in the halo population is not matched by a decrease of the strahl population at these distances, as has been reported for previous observations at distances greater than 0.3 au. We also find that the halo is negligible at small heliocentric distances. The fractional strahl density remains relatively constant $\sim$1% below 0.2 au, suggesting that the rise in the relative halo density is not solely due to the transfer of strahl electrons into the halo.

*Keywords:* Sun — Heliosphere — Plasma physics — solar wind

Corresponding author: Joel B Abraham
joel.abraham.19@ucl.ac.uk

## 1. INTRODUCTION

The solar wind is a highly ionised plasma consisting of protons, $\alpha$-particles, trace amounts of heavier ions, and electrons flowing continuously out of the corona and filling the heliosphere. The ions contribute to most of the solar-wind mass and momentum fluxes due to their heavier mass, while the relatively light electrons play a key role in solar-wind dynamics as the main carrier of heat flux due to their much larger thermal speeds (Marsch 2006). In collisional plasmas Coulomb collisions maintain local thermodynamic equilibrium (Feldman et al. 1975). However, the solar wind is mostly collisionless, which means that, above a certain energy, the particle velocity distribution function (VDF) can deviate from that of a classical isotropic Maxwellian equilibrium distribution. Decades of solar wind observations at heliocentric distances greater than 0.3 au have shown that the electrons in the solar wind can often be categorised into three distinct populations: the core, the halo and the strahl (Feldman et al. 1975; Maksimovic et al. 2005; Štverák et al. 2009). The core represents the thermal part of the overall electron distribution with energy $\leq$ 50 eV. It is usually described by a (bi-)Maxwellian distribution function at 1 au (e.g., Štverák et al. 2009). The core contains 90-95% of the total local electron density (Maksimovic et al. 2005). The Maxwellian nature of the core is attributed to collisions. At higher energies, at which collisions are less effective, non-equilibrium structures such as beams and high-energy tails can develop and survive. The halo and strahl populations represent the electrons in the suprathermal energy range ($\geq$ 50 eV). The halo exhibits a greater temperature and an enhanced high-energy tail compared to the Maxwellian core distribution. It is often characterized as a (bi-)$\kappa$ distribution (e.g., Štverák et al. 2009). The core and the halo are quasi-isotropic and thus show significant particles fluxes at all pitch angles. Conversely, the strahl is usually seen as a collimated, magnetic-field-aligned beam of electrons in the suprathermal energy range, moving parallel, or anti-parallel, to the local magnetic field (Gosling et al. 1987). The strahl population is more often seen in the fast wind compared to the slow wind (Rosenbauer et al. 1977).

Due to their weak collisionality, suprathermal electrons preserve some of their coronal characteristics and thus convey information about their coronal source regions (Scudder & Olbert 1979; Berčič et al. 2020). Therefore, precise descriptions of the electron VDF and its evolution are fundamental to determining the processes responsible for the solar wind acceleration (Jockers 1970; Zouganelis et al. 2004; Maksimovic et al. 1997; Lemaire & Scherer 1971). For example, the exospheric theory of the solar wind assumes the electron distribution to be collisionless above the exobase. It predicts that the electron VDF evolution through the heliosphere is driven by velocity filtration and ambipolar diffusion created by the interplanetary electric field (Maksimovic et al. 1997). Even though this model predicts the acceleration of the solar wind, the observed nature of the electron VDF in the heliosphere shows some inconsistencies with its predictions (Maksimovic et al. 2001). However, Lie-Svendsen

et al. (1997) modified the model by solving the Boltzmann equation with the Fokker Planck approximation for collisions and were able to produce results showing a strahl population consistent with that observed at 0.3 au, but with no halo present.

On average, the evolution of the core density,$n_c$, with radial distance,$r$, is in excellent agreement with expectations for an isotropically expanding gas, for which $n \propto r^{-2}$. In contrast, the halo and strahl populations show more complex density profiles than a steady radial expansion from 0.3 - 4 au (Štverák et al. 2009; Maksimovic et al. 2005). Under purely adiabatic conditions, the strahl population would continue to narrow in pitch angle as it propagates radially away from the Sun into regions of lower magnetic field strength, due to conservation of the magnetic moment. However, this is not generally observed, and the strahl appears to undergo significant pitch-angle scattering, as its width gradually increases with radial distance (Anderson et al. 2012; Hammond et al. 1996; Graham et al. 2017). In a simple model, Owens et al. (2008) examine the combined effects of adiabatic focusing and a constant rate of scattering on the electron populations. According to this model, a constant scattering rate dominates over the adiabatic focusing beyond $\sim 0.1$ au, and the strahl pitch-angle width thus increases with heliocentric distance. Moreover, the strahl parallel temperature does not vary with radial distance close to the Sun (Berčič et al. 2020), which supports the assumption that the strahl carries information about the coronal temperature. However, the exact physics of the origin of the strahl is still unclear.

The origin of the radial evolution of the halo parameters remains elusive, although beam instabilities and resonant wave–particle interactions are potential mechanisms for the scattering of strahl electrons into the halo, while leaving the core relatively unaffected (Vocks et al. 2005; Saito & Gary 2007). Alternatively, Coulomb collisions (Horaites et al. 2017) or background turbulence (Saito & Gary 2007) can play similar roles in the evolution of the halo.

The solar wind near the Sun is more pristine, or less processed by transport related effects, which means that the electron distribution function is likely to be closer to the original distribution in the outer corona of the Sun. Comparing electron distributions at different distances from the Sun with those recorded very close to the Sun enables us to improve our understanding of processes which facilitate solar wind acceleration and heating. At the same time, it allows us to probe the mechanisms that modify the distribution as the solar wind travels to greater heliocentric distances. We present the evolution of macroscopic quantities such as the density and temperature of the thermal and suprathermal populations at heliocentric distances below 0.3 au which has not been examined using data from missions launched prior to Parker Solar Probe.

In this paper, we develop a fitting routine, which in part uses machine learning, to fit the electron VDFs measured by NASA's Parker Solar Probe (PSP) to model distributions for the core, halo and strahl during PSP's near-Sun encounters 2 through 5. Building on similar work by Maksimovic et al. (2005), Štverák et al. (2009) and Halekas et al. (2020), we extend the observational range to cover the region from

$\sim$0.13 au to 0.5 au, and use higher time resolution data from PSP, to further examine the nature and evolution of the three electron populations. In Section 2, we discuss our preparation of the PSP data, and in Section 3, we describe our fitting routine and the machine learning algorithm to determine breakpoints in the distributions. Our results are presented in Section 4. We then discuss the results in Section 5 in the context of previous measurements at greater heliocentric distances. We finally provide a summary and conclusions in Section 6.

## 2. DATA HANDLING

PSP was launched in August 2018 and will eventually achieve a closest perihelion distance of 9.86 solar radii (Rs) in 2024, giving us unprecedented measurements of the Suns corona. Our analysis addresses observations over four perihelia passes or 'encounters' (encounter 2 (30/03/2019 – 10/04/2019), encounter 3 (16/08/2019 - 20/09/2019), encounter 4 (24/01/2020 – 04/02/2020) and encounter 5 (20/05/2020 -15/06/2020)). During the data intervals used in this study, PSP's closest perihelion is at a heliocentric distance of 0.13 au (27 Solar radii).

For the main part of our analysis, we use data from the Solar Wind Electrons, Alphas and Protons (SWEAP, Kasper et al. 2016) instrument suite. SWEAP measures the 3D electron VDF with the Solar Probe ANalyzer - Electron (SPAN-E) sensor consisting of two top-hat electrostatic analysers (ESAs): SPAN-A and SPAN-B. Together, the two ESAs measure electrons arriving from across almost the full sky using orthogonally positioned $120^\circ \times 240^\circ$ fields of view (FOV), over an energy range from 2 eV to 1793 eV during our measurement intervals. SPAN-A is located on the anti-ram side of the spacecraft and SPAN-B is located on the ram side. Each ESA samples over 16 azimuth, 8 elevation, and 32 energy bins. The azimuth resolution of each sensor is either 6 degrees or 24 degrees depending on the look direction, and covers a total of 240 degrees. The elevation has a resolution of $\sim 20^\circ$. SPAN-A and SPAN-B each contain a mechanical attenuator system, which consists of a series of slits that are engaged when the particle counts approach the sensor saturation limits. During periods of attenuation, the total particle flux is reduced by a factor of 10. SPAN-E electron VDF measurements during encounters typically have a measurement cadence of 13.98 seconds. More details about the operational modes of SPAN-E are described in Whittlesey et al. (2020).

In this work, we use SPAN electron (SPAN-E) level 3 pitch-angle data. The level 3 data are provided in 32 energy bins and in twelve pitch-angle bins of width $15^\circ$ with bin centres ranging from 7.5 to $172.5^\circ$. In the production of the level 3 dataset, the measurements from both sensors (SPAN-A and SPAN-B) are re-sampled from their intrinsic resolution onto this pitch angle grid which eliminates each instrument pixel one count effects. These level 3 data are provided in units of differential energy flux ($\mathrm{cm^{-2}\,s^{-1}\,str^{-1}\,eV^{-1}eV}$).

In order to distinguish between solar-wind streams with different bulk speeds, we use data from SWEAP's Solar Probe Cup (SPC) sensor and SPAN-i. We utilise the SPC sensor to obtain the proton bulk speed moment denoted as `wp_moment` for encounters two and three (Case et al. 2020). The SPC is a Faraday cup that is mounted near the spacecraft heat shield. The SPC measurement cadence is higher than SPAN-E's, and thus in this work, our SPC moments are averaged over the SPAN-E integration times. We also use the proton bulk speed values for encounters four and five using fits to the proton measurements from SPAN-i.

We perform bi-Maxwellian fits to the proton core distribution function from the `spi_sf00_8dx32ex8a` data product, observed by SPAN-i, using the methodology described by Woodham et al. (2020), based on earlier routines developed by Stansby et al. (2018). Only the proton core speed is used from these fits in this work. The proton measurement cadence is higher than SPAN-E's and thus in this work the values are averaged over the SPAN-E integration times.

Parts of distribution are missing due to spacecraft obstruction.To mitigate for this, we remove any VDFs for which more than 20% of the data are missing. The level 3 data are converted from differential energy flux to the phase space density through

$$f(v_{\parallel}, v_{\perp}) = \frac{m_e}{V^2} J(E, \alpha) \mathrm{d}A \, \mathrm{d}\Omega \, \mathrm{d}E \, \mathrm{d}t, \tag{1}$$

where $f$ is the phase space density, V is the velocity $J$ is the differential energy flux (DEF), $\Omega$ is the solid angle, d$t$ is the acquisition time per elevation and energy bin.

As PSP approaches the Sun, the UV radiation reaching the spacecraft surface generates increasing numbers of secondary electrons which affect the lower energy bins. Halekas et al. (2020) account for these lower energy secondary electrons in their fitting model by assuming the secondary electrons have a Maxwellian distribution with a fixed temperature of 3.5 eV. As our data set spanned over 2 years we have noted large variations in the nature of the secondary electrons. In our fitting procedure, to avoid the effects of secondary electrons especially during the encounters, we have thus ignored all data points associated with energies below 30 eV. This selection criterion makes core-temperature measurements below 30 eV less reliable than measurements at larger core temperatures.

## 3. DISTRIBUTION FITTING

The fitting technique is widely used in solar and space plasma physics in order to derive plasma bulk parameters from observations (Halekas et al. 2020; Berčič et al. 2020; Nicolaou et al. 2020; Stansby et al. 2018; Štverák et al. 2009; Maksimovic et al. 2005).To capture the properties of the electrons, we analytically describe the anticipated distribution function and then fit to the measured data. Once fitted, we obtain parameters such as density, temperature, and bulk speed of each modelled population. Similar to Maksimovic et al. (2005), we fit the core electrons with a bi-Maxwellian function in the magnetic field aligned frame, while we fit a bi-$\kappa$ function

to the halo population. Once the core and halo were fitted, Maksimovic et al. (2005) subtracted the resulting core-halo distribution model from the observed distribution. They integrated the remaining population in velocity space to obtain macroscopic strahl properties. Štverák et al. (2009) performed a similar fitting routine, but modified it by fitting the suprathermal components with a truncated model, such that suprathermal components are restricted to the suprathermal parts of velocity space. Both studies show that the non-thermal halo population is modelled well by a bi-$\kappa$ and the core by a bi-Maxwellian, but Štverák et al. (2009) applied a different methodology, using a truncated $\kappa$-model to represent the strahl. This shows that closer to the Sun, the $\kappa$ index of the strahl population approaches a value of 10, which provides a distribution that is close to a Maxwellian. In our fit model, we employ machine learning to determine the break-point energies of the measured distribution and then use these in the fitting routine to constrain the fits, as described in section 3.1. The breakpoint energy is defined as the energy at which the nonthermal structures deviate from the thermal Maxwellian distribution (Feldman et al. 1975; Štverák et al. 2009).We discuss the fitting routine in section 3.2 and the error analysis in section 3.3.

### 3.1. *Determination of breakpoints through machine learning*

As our fitting routine uses the breakpoint energy between the core and halo as an input, we employ the machine learning techniques described by Bakrania et al. (2020) that use unsupervised learning algorithms to determine these breakpoint energies. We also use these techniques to separate halo and strahl electrons in pitch angle and energy space. This technique uses the K-means clustering method (Arthur 2007) from the `scikit-learn` library (Pedregosa et al. 2011). K-means clustering works by grouping a set of observations into K clusters, based on similarities between the observations. Unsupervised learning algorithms do not require the user to assign labels to training data, thereby reducing bias (Arthur 2007). In our method, we manually set the number of clusters in the K-means algorithm to 2, which represents the core cluster and a suprathermal cluster. The algorithm calculates the breakpoint energy at a specific pitch angle by separating the energy distributions, at that pitch angle, into two clusters with the mid-point determined to be the breakpoint energy.

The K-means algorithm clusters these energy distributions by minimising the function:

$$\sum_{i=1}^{u} \sum_{j=1}^{K=2} \omega_{ij} \left\| x_i - \mu_j \right\|^2, \tag{2}$$

where

$$\mu_j = \frac{\sum_{i=1}^{u} \omega_{ij} x_i}{\sum_{i=1}^{u} \omega_{ij}}, \tag{3}$$

$$\omega_{ij} = \begin{cases} 1 & \text{if } x_i \text{ belongs to cluster } j \\ 0 & \text{otherwise,} \end{cases} \tag{4}$$

and $u$ is the number of 3-tuples at the defined pitch angle. In Eq. (2), $x_i$ is defined as the vector representation of the differential energy flux tuples, where the index $i$ indicates tuples of three adjacent energy bins (i.e., energy distributions which range across three energy bins). The variable $\mu_j$ is the vector representation of two random DEF tuples, where the index $j$ labels each cluster. The K-means algorithm calculates the breakpoint energy by: (1) randomly selecting two DEF vectors to become the central points, or 'centroids' of each cluster, $\mu_j$, (2) allocating each DEF vector, $x_i$, to its nearest centroid, by finding the smallest least-square error between that vector and the centroids, (3) determining new centroids, $\mu_j$, by averaging the DEF vectors assigned to each of the previous centroid, (4) re-allocating each DEF vector, $x_i$, to its new closest centroid, $\mu_j$, and (5) repeating steps 3 and 4 until no more new re-allocations occur. After the algorithm has computed the two clusters, the breakpoint energy at the relevant pitch angle is calculated as the center between the highest energy bin in the lower energy cluster (which represents the core), and lowest energy bin in the higher energy cluster (which represents the suprathermal populations).

In order to distinguish between strahl and halo electrons, we apply this method to both pitch angle and energy distributions. The method used for distinguishing between pitch angle distributions is analogous to the method described above, with $x_i$ now defining a pitch angle distribution at a certain energy. However the K-means algorithm is now finding the 'break' in pitch angle. A detailed description of this method and an analysis of its effectiveness is provided by Bakrania et al. (2020). Arthur (2007) details a comprehensive and more general account of the K-means algorithm.

After applying this method, the K-means algorithm outputs a list of pitch angle bins, energy bins, and time-stamps which characterise the transition from core to suprathermal electrons. With these outputs we obtain a set of parameters, including times when a strahl is present, strahl energies, and widths, which we use to constrain our fitting analysis.

### 3.2. *Fitting of the VDF*

We fit the observed distribution functions with the sum of three analytical expressions which separately describe each of the electron populations, namely the core, halo and strahl:

$$f_e = f_c + f_h + f_s, \tag{5}$$

where $f_c$ is the fitted core, $f_h$ is the fitted halo, $f_s$ is the fitted strahl. Following on from previous work (Maksimovic et al. 2005; Štverák et al. 2009; Halekas et al. 2020; Berčič et al. 2020), the core electrons are modelled with a 2 dimensional bi-Maxwellian distribution function:

$$f_c = \frac{N_c}{\pi^{3/2} V_{\parallel \omega c} V_{\perp \omega c}^2} \exp\left( -\frac{V_\parallel^2}{V_{\parallel \omega c}^2} - \frac{V_\perp^2}{V_{\perp \omega c}^2} \right), \tag{6}$$

where $N_c$ is the core density, $V_{\parallel_{\omega c}}$ is the core parallel thermal velocity, $V_{\perp_{\omega c}}$ is the core perpendicular thermal velocity. For the halo population, we fit to a bi-$\kappa$ function:

$$f_h = \frac{N_h}{V_{\parallel_{\omega h}} V_{\perp_{\omega h}}^2} \left(\frac{2}{\pi(2\kappa-3)}\right)^{3/2} \frac{\Gamma(\kappa+1)}{\Gamma(\kappa-\frac{1}{2})} \left[1 + \frac{2}{2\kappa-3}\left(\frac{V_\parallel^2}{V_{\parallel_{\omega h}}^2} + \frac{V_\perp^2}{V_{\perp_{\omega h}}^2}\right)\right]^{-(\kappa+1)}, \quad (7)$$

where $N_h$ is the halo density, $V_{\parallel_{\omega h}}$ is the halo parallel thermal velocity, $V_{\perp_{\omega h}}$ is the halo perpendicular thermal velocity, and $\kappa$ is the $\kappa$ index. For the strahl component, we use a modification to the previous works cited above and fit to a bi-Maxwellian drifting in the parallel direction at speed $U_{\parallel_s}$ with respect to the magnetic field. Thus, the strahl is described by

$$f_s = \frac{N_s}{\pi^{3/2} V_{\parallel_{\omega s}} V_{\perp_{\omega s}^2}} \exp\left(-\frac{(V_\parallel - U_{\parallel_s})^2}{V_{\parallel_{\omega s}}^2} - \frac{V_\perp^2}{V_{\perp\omega s}^2}\right), \quad (8)$$

where $N_s$ is the strahl density, $V_{\parallel_{\omega s}}$ is the strahl parallel thermal velocity, $V_{\perp_{\omega s}}$ is the strahl perpendicular thermal velocity, and $U_{\parallel_s}$ is the strahl parallel bulk velocity.

As there are 11 free parameters involved in the fit ($N_c$, $N_h$, $N_s$, $V_{\parallel_{\omega c}}$, $V_{\perp_{\omega c}}$, $V_{\parallel_{\omega h}}$, $V_{\perp_{\omega h}}$, $\kappa$, $V_{\parallel_{\omega s}}$, $V_{\perp_{\omega s}}$, $U_{\parallel_s}$), we split our fitting process into two stages. This has the advantage of reducing the number of nonphysical fits which can arise due to the large number of degrees of freedom. The first stage is to fit only to the core + halo model and then fit to the strahl model. An example of the results of this stage are shown in the left panel of Figure 1, which presents the core and halo fits (blue and red lines respectively) to the data points from a single measured distribution (purple diamonds). In the second stage, we use the core-strahl breakpoint energy from our machine learning algorithm to constrain the relevant velocity space of the strahl electron population. This second fit captures the strahl using the drifting Maxwellian model, with the outputs of the first fit for the core and halo parameters and the strahl break point energy as fixed inputs to constrain the velocity space. The right panel of Figure 1 presents the results of this strahl fit (yellow line) for the example distribution, plotted on top of the core and halo fits and the data points from the left panel. The overall fit is shown as the green trace, and from visual inspection it can be seen that a reasonable overall fit is achieved.

The fits are performed using the Levenberg–Marquardt fitting algorithm in log-space to capture the 2D electron distribution function in the field aligned velocity space (Levenberg 1944) with each point weighted with the errors described in section 3.3. The free parameters are constrained as follows: core, halo and strahl density must be greater than 0; the strahl parallel bulk velocity must be less than $2.5 \times 10^7\,\mathrm{m\,s^{-1}}$; and $\kappa$ must be greater than 1.5 and less than 25.

A goodness of fit parameter is evaluated by comparing measured and modelled points along the perpendicular direction, as it is expected that there is no strahl present at these pitch angles, and along the parallel or anti-parallel direction which does not have the strahl (i.e, the anti-strahl direction). This allows us to capture the

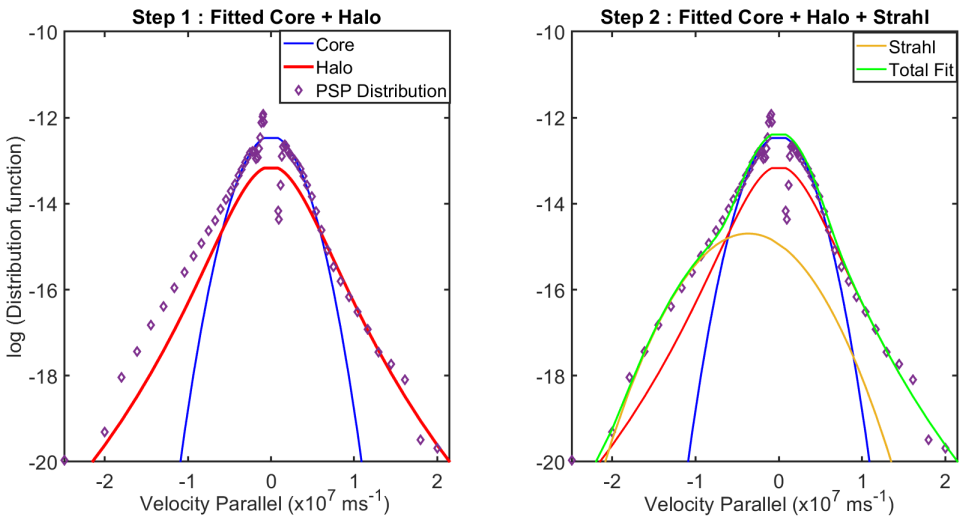


**Figure 1.** Two-step fitting process. The purple diamonds mark the measured distribution at 0.2940 au on $25^{th}$ Aug 2019 at 03:28:28 UT, red the fit for the bi-Maxwellian core, and blue fit for the bi-kappa halo. The gold line represent the fit for the drifiting bi-Maxwellian strahl. The panel on the left shows the core and halo fit for the measured distribution. The second fit is shown in the right-hand panel where the strahl is fitted. The green line represents the total fit.

anisotropic nature of the core and halo populations. To evaluate the overall goodness of the fit, we evaluate the reduced $\chi^2$ parameter:

$$\chi^2 = \frac{1}{n-m}\sum_i \frac{(O_i - C_i)^2}{\sigma^2}, \tag{9}$$

where $O_i = \log(\tilde{f}_i/1s^3m^{-6})$ are the measured data based on the measured full distribution function $\tilde{f}_i$, $C_i = \log(f_e/1s^3m^{-6})$ are the fitted data, $n$ is the number of fitted data points, $m$ is the number of variables to fit and $\sigma^2$ is the variance of $\log(f)$.

We assume that the bulk speeds of the core and halo populations are zero in our fit models in the instrument frame. Consequently, any measured distributions with significant non-zero drifts will manifest as a large reduced $\chi^2$ value and would be excluded from the analysis. Once that is done, we undertake the analysis of the features of the suprathermal populations by taking partial moments of the fitted curve by integrating over the part of velocity space constrained by the breakpoints obtained from the machine learning algorithm described in Section 3.1.

### 3.3. *Error Analysis*

We model the overall measurement error as a combination of that given by Poisson statistics, combined with an additional error which reflects the likely systematic error in the instrument measurement, arising due to the finite MCP efficiency and uncertainty in other instrumental effects, which we combine and capture here as an effective overall uncertainty in the instrument geometric factor. The Poisson error is the dominant error source when the number of counts is small. We quantify the rela-

tive error in the geometric factor as 10 %, a value which has been adopted following direct discussions with the data provider team.

In the creation of the SWEAP VDF data, the value of the distribution function $f$ at a given energy, azimuth, and elevation is calculated based on the raw counts $C$ as :

$$f = \frac{{m_e}^2 C}{2\,\Delta t\, E^2 G}, \tag{10}$$

where $\Delta t$ is the counter readout time, $G$ is the geometric factor, and $E$ is the energy. Based on Gaussian error propagation, the Poisson error and the geometric factor uncertainty lead to the following result for the variance of the data points (i.e., of $\log(f)$) in our measured distribution function:

$$\sigma^2 = \left(\frac{m_e}{\ln(10) E \sqrt{2\,\Delta t\, G f}}\right)^2 + \left(\frac{1}{\ln(10)}\frac{\Delta G}{G}\right)^2, \tag{11}$$

where $\Delta G/G = 0.1$ is the relative error in the geometric factor. In our analysis, we only include fits that have a $\chi^2 \leq 1$.

Overall, we have examined over 450,000 electron velocity distribution functions obtained by PSP SWEAP from the years 2019 and 2020. After applying the $\chi^2$ limit and further removal of some clearly nonphysical fits, we obtain $\sim$ 300,000 fits for further analysis, of which 220,000 fits have an associated solar wind speed measurement from SPC or SPAN-i.

## 4. RESULTS

Most of the data measured during this time period has speeds less than $400\,\mathrm{km\,s^{-1}}$ which we classify as the slow wind. We split the data into 50 equal-width radial distance bins, and the median value of a given parameter of interest in each radial distance bin is calculated. We calculated the the upper and lower error bar for each radial distance bin as the upper and lower quartile respectively.

Figure 2 shows the radial evolution of the averaged fitted parameters. Panel (a) of the Figure shows the averaged core density as a function of the heliocentric distance. This is broadly in line with the expectations for a radial isotropic expansion of this population. The $r^{-2}$ trend is represented by the solid green curve. Below 0.2 au, the halo density (panel (b)) shows only a moderate dependence on heliocentric distance within the error bars. However, over the same radial distance range, the strahl density (panel (c)) has a clearly steeper gradient which is more significant.

The thermal speed of the fitted core distribution (panel (e)) decreases with radial distance in this range.The thermal speed of the fitted halo distribution initially increases from $2.2 \times 10^6 ms^{-1}$ at 0.13 au to $3.5 \times 10^6 ms^{-1}$ at 0.23 au and thereafter the thermal speed decrease. The parallel thermal velocity is enhanced above the perpendicular at all distances shown, indicating a persistent anisotropy in the parallel direction for the halo population.

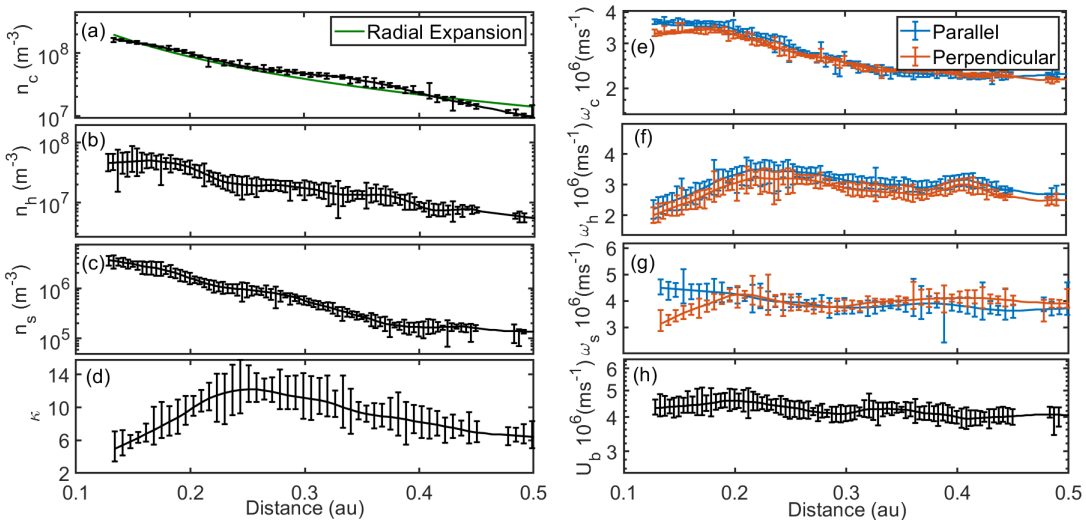


**Figure 2.** The radial evolution of the fit results for solar wind in the speed regime less than 400 $kms^{-1}$.Panel (a) shows the radial evolution of the core density and the black dashed line shows the expected evolution of a isotropically expanding gas. Panel (b) and (c) represents the radial evolution of the halo and strahl population respectively. Panel (d) shows the radial evolution of the kappa value for the fitted halo population. Panel (e),(f) and (g) represents parallel and perpendicular thermal speeds of the core, halo and the strahl respectively. Panel (h) shows the radial evolution of the strahl bulk parallel thermal speed.

The radial evolution of the kappa value for the fitted halo distribution is shown in panel (d). The kappa parameter provides a measure of the non-thermal state of the halo population. As kappa tends to infinity the distribution becomes closer to a Maxwellian. For the slow solar wind regime shown here, the kappa value is low at $\sim$ 4 for the lowest distances sampled. The kappa value rises from $\sim$4 to $\sim$12 between 0.13 au and $\sim$ 0.24 au before the steadily decreaseing over the rest of the distance range shown.

We also observe that the fit to the strahl component shows a strong decrease in density with distance in both solar wind regimes (panels (c)). The strahl thermal speed component is $V_{\parallel \omega s} > V_{\perp \omega s}$ closer to the Sun, which slowly decreases with radial distance, such that this distribution is isotropic (within error bars) by $\sim$0.2 AU. unlike the core and halo which both show clear declines as distance increases.

To examine the complex radial evolution of the suprathermal population. We numerically integrate the total fitted curve over velocity space using the breakpoints to define the energy and/or pitch angle limits for the core, halo and strahl populations. In Figure 3 we present the integrated density evolution of the three electron populations on a common scale with heliocentric distance. Here the integrated core density data are shown in blue, the integrated halo density in orange and the integrated strahl density in yellow. The two suprathermal populations are at least an order of magnitude lower in density than the core population across the entire distance range shown. As mentioned above the core density falls as $r^{-2}$ up to 0.25 au. From 0.25 au, we note a deviation of the core electron population from the radial expansion line.

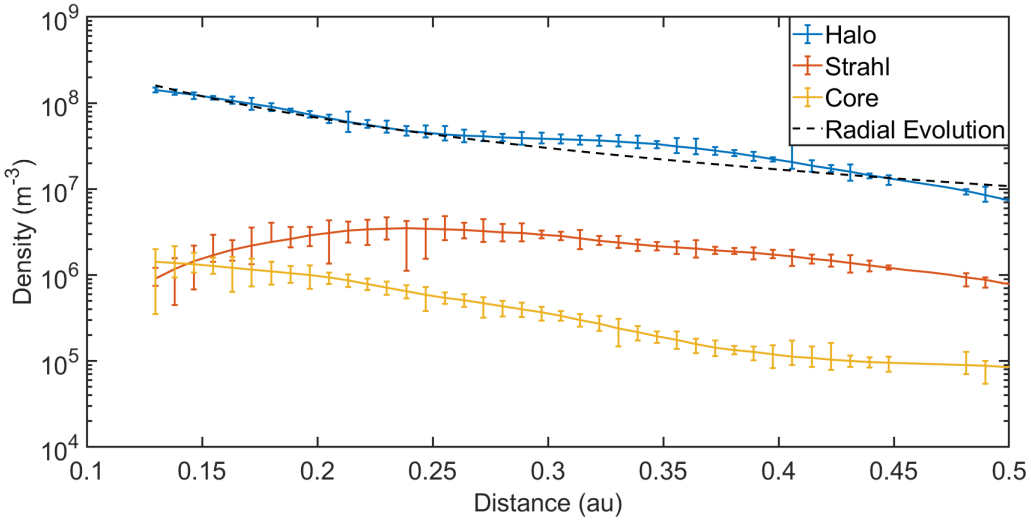


**Figure 3.** The blue line is the core density, the orange line is the halo density, the yellow line is the halo, the black dashed line is theoretical line for an isotropically expanding gas.

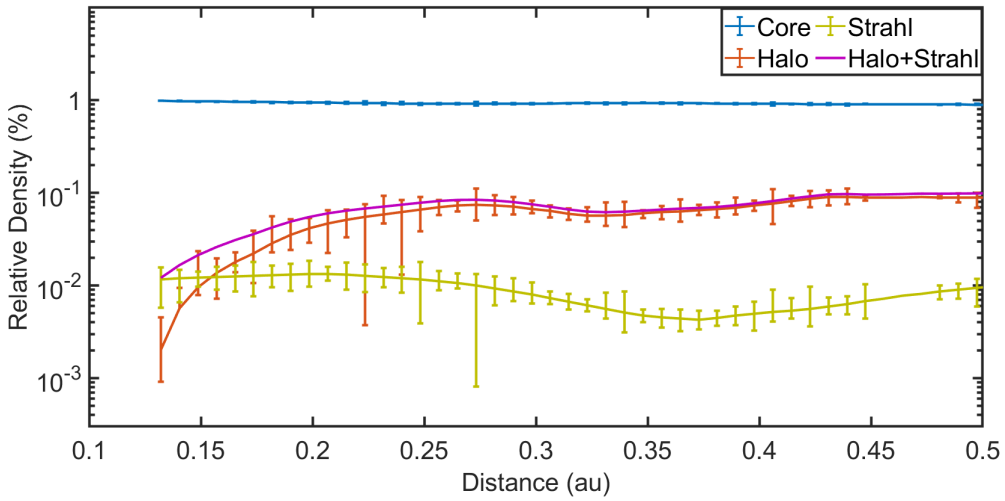


**Figure 4.** The blue line is the core density, the orange line is the halo density, the green line is the strahl density and the purple line is the total suprathermal population.

Figure 3 also shows that from 0.2 au outwards the halo (orange line) makes up most of the suprathermal population, while the strahl makes up most of the suprathermal population below 0.2 au. Figure 3 also shows that the evolution of the suprathermal population with radial distance does not follow a $r^{-2}$ trend.Below 0.25 au we see that the halo density decrease with radial distance while there is a small increase in the strahl density. From 0.25 au onwards, both populations show a steady decline in density with increasing radial distance.

To remove the effects of expansion, we look at the relative densities of the 3 electron populations with respect to the total local electron density in a similar way to (Štverák et al. 2009). Figure 4 shows the relative density of the core population is

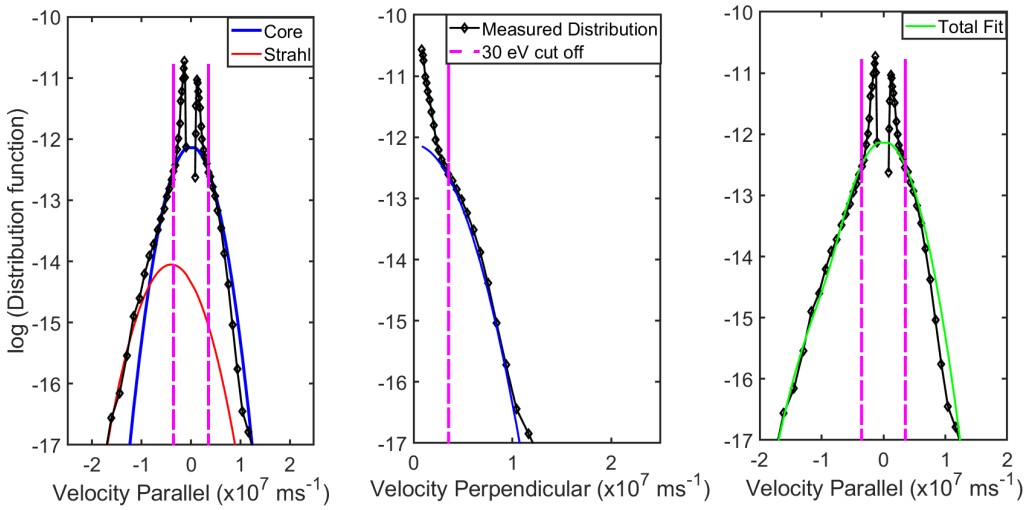


**Figure 5.** A representative distribution recorded at a distance of ∼0.13 au.The black trace with diamonds shows the measured distribution. The blue trace represents the output of our fitting routine for a Maxwellian core, and the red trace represents the output for the fit to a Maxwellian strahl drifting along the B-field direction. The pink vertical dashed lines represent the 30 eV measurement energy below which we do not fit to data due to secondary contamination, as discussed in the text. The left hand panel shows a cut along the parallel velocity direction, while the middle panel shows the cut along $V_{\|}$=0 in the perpendicular direction. In the right-hand panel, the green trace shows the final combined fitted curve to the measured distribution. Note that this panel indicates an excellent fit to the data without the need to infer a third fit for the halo model, such that the halo contribution to this fit is negligible.

above 90% across the full distance range sampled. Thus, the combined density of the suprathermal populations (shown in these plots by the purple line) makes up less than 10% of the total electron density observed at any distance. From 0.124 au to 0.2 au the relative halo density (orange line) increases from less than 1% to ∼ 10% of the total electron density in all cases. Between 0.15 and 0.2 au there is a point in each plot at which the relative halo density is equal to the relative strahl density, which we will refer to as the *halo-strahl cross-over point* in this paper. It is not straightforward to determine the exact location of the halo-strahl cross-over point due to the size and overlaps in the error bars. The relative strahl density stays approximately constant (∼1%) below 0.2 au but there is a sharp rise in relative halo density from less than 1% to ∼7%. The total fractional density of the combined suprathermal populations rises from ∼ 1% at the closest distances sampled (∼0.13 au) to almost 10% above 0.25 au.

To examine this in more detail, we looked at the average shape of the distribution function below the halo-strahl cross-over point. For this selection of data, most of the VDFs can be described well with just the core and strahl elements of the model fit, with no explicit need to include a halo model, as seen from the example distribution/fits illustrated in Figure 5.

## 5. DISCUSSION

The relative densities and radial trends of properties of the core electron population are broadly in agreement with previous observations by Maksimovic et al. (2005) and Štverák et al. (2009) for distances $\gtrsim 0.28$ au. These authors demonstrated, for this distance range, that the relative density of the strahl is greater than the relative density of the halo closer to the Sun ($\sim$ below 0.6 AU). Contrary to these previous results, our observations show that the relative density of the two suprathermal electron populations does not evolve in an inverse manner below 0.3 au, where the strahl density decreases as the halo density increases. Below 0.2 au the total fractional density of the suprathermal population is not constant, but drops from $\sim$ 10% to $\sim$ 1%. This would imply that with increasing distance from the Sun there must be some process or processes drive an increases in the total number of electrons in the suprathermal energy range. A candidate source for these electrons would be the core in this region. If this is the case then it is possible that the quasi-isotropic nature of the halo could be explained by a process which creates the halo from the core population. Extrapolating the lines in Figure 4 to distances closer to the Sun, we notice for the slow solar wind the distribution function would be composed of a core and a strahl model without a significant halo component.

The fact that the fractional strahl density remained relatively constant $\sim$1% and fractional halo density increased from less than 1% at 0.124 au to $\sim$7% at 0.2 au shows that the halo cannot just be formed from the scattering of strahl alone as suggested by (Štverák et al. 2009). Thus, there appears to be more than one process contributing to the growth of the halo population. This may be a multi-stage process in which, say, a fraction of the core population is accelerated to suprathermal energies by a resonant wave-particle interaction or other plasma processes. Alternatively, larger scale dynamics may play a role, such as the field-aligned acceleration of reconnection outflow beams, followed by scattering in pitch angle to form the halo. Further analysis is needed to confirm the nature of any such coupling between the core and the suprathermal population. We also define the *halo strahl cross over* point, described above as the point where the halo density and strahl density are equal. Below the *halo strahl cross over* point most of the suprathermal population is moving along the field line while above this point most of the suprathermal population is present at all pitch angles. This point maybe important in the study of processes that concern the evolution of the suprathermal populations. However, the fractional trends in Figure 3 show that the total suprathermal population continues to decrease in the same radial range.

We have also specifically examined electron VDFs which were recorded at radial distances below the the *halo strahl cross over* point. Electron distributions below 0.15 au can in general be well described with only a core and a strahl model as shown by Figure 5. Another feature we often note at the closest distances sampled is a deficit in the measured distribution function, with reference to the core fit, in the anti-strahl direction. Halekas et al. (2020) examined the first 2 orbits and reported

a similar truncation in the Maxwellian. This deficit is not included explicitly by our model, and this means the core density estimate at the closest distances to the Sun maybe slightly overestimated. If the deficit is sufficiently large then this should result in a large reduced sum of the squares and be discarded from our analysis.

Another interesting result from our analysis is the variation in the $\kappa$ value with radial distance. The variation in $\kappa$ indicates the changes in the shape of the high energy tails with radial distance. At the closest distance sampled, the $\kappa$ value is $\sim 3$ and rises to 6 around 0.25 au. When we compare this rise in $\kappa$ with the halo density trend shown by Figure 4 we notice that the halo density was less than 0.01 % and rises to a few percent.

From panel (e) to (g) of Figure 2, we observe the non-adiabatic nature of the slow solar wind. At the closest distance sampled there seems to be a persistent anisotropy in all three electron populations with the strahl exhibiting the strongest parallel anisotropy. The core population cools with radial distance but with gradients in the thermal speed. This shows that the cooling rate varies with radial distance while remaining quasi-isotropic with the thermal speeds within the error bars. However,the halo thermal speed initially rises from $2 \times 10^6 ms{-}1$ at 0.13au to $3.7 \times 10^6 ms^{-1}$ at 0.25 au and then decreases with radial distance. The initial rise can be attributed to the growth of the halo as more particles populate the upper halo energy range. We are unaware of any theory that explains these thermal trends. Further research into what drives the global thermal trends in needed.

As evident from Figure 2, the strahl parallel thermal velocity does not vary with radial distance when fitted to a drifting bi-Maxwellian model. This result has also been reported by Berčič et al. (2020). This result is consistent with a recent kinetic model for the strahl evolution in the inner heliosphere, which also shows that the strahl parallel temperature and bulk velocity are constant with heliocentric distance (Jeong et al. 2022). In exospheric models, the strahl is believed to carry information about the exobase (Jockers 1970), which means that the constant strahl parallel temperature and bulk speed provides critical information about the coronal electrons at its origin. The strahl parallel thermal speed from our fits is approximately the same magnitude as the typical temperature on the corona ($\approx 10^6$ K). Further analysis of data closer to the Sun obtained from future PSP encounters will be needed to confirm whether the strahl parallel temperature indeed preserves the coronal electron temperature. The core and strahl have a parallel anisotropy closer to the Sun at 0.13 au, but this anisotropy decreases with radial distance and approaches isotropy within the statistical errors. Another new finding we show with our work is that the strahl parallel bulk speed stays roughly constant within the error bars. This means that the strahl could be a useful indicator of the origins of the source regions of the solar wind.

In exospheric solar wind models, the electrons with energy less than the electric potential at a given radial distance are reflected and are trapped in a potential well

(Maksimovic et al. 2001). The deficit in the distribution function that we observe in the anti-strahl direction could then be a result of this trapping boundary. However in this theory, this cut-off in the distribution is quasi-discontinuous, while we observe a smoother drop below the Maxwellian VDF values in the sunward side of the VDF. We also observe this signature becomes weaker with radial distance. This change in the signature maybe explained by collisions which are usually ignored by exospheric models. Regardless, more research is required to better understand these deficits by quantifying the point where the Maxwellian truncates, since they potentially give insight into the role of the interplanetary electrostatic potential for the acceleration of the solar wind.

## 6. CONCLUSIONS

We have applied a new fitting routine to electron VDF measurements, which for the first time incorporates breakpoint energies obtained from a machine learning algorithm (Bakrania et al. 2020). This new technique was applied to a large data set of PSP SPAN observations at varying distance from the Sun. We use our fitting results to investigate the evolution of the core, halo and strahl for encounters 2, 3, 4, and 5. We have shown that the core makes up more than 90% of the total electron density for all the distances sampled, whereas the non thermal electrons make up less than 10%, as previously observed for distance $> 0.3$ au (Maksimovic et al. 2005; Štverák et al. 2009; Halekas et al. 2020). The radial $r^{-2}$ dependence of the core population extends below 0.3 au. We also show that the relative suprathermal population increases from the $\sim 1\%$ at the closest distances sampled to $\sim 10\%$ around 0.22 au, which indicates that there is a relative increase in the non-thermal particle densities over the inner regions of the heliosphere.

Our analysis does not reveal a distinct inverse relationship between the halo and strahl population below 0.25 au. Rather, we find that the strahl density stays approximately constant whilst the halo density increases. We introduce a point called the *halo strahl cross over* point,where the relative halo density is equal to the relative strahl density.At the closest distances sampled below this point, the distribution can generally be well modelled with only a core and strahl model with little/no contribution from the halo model.The low halo density closer to the Sun suggests the halo is diffused and drops below the one count sensitivity level of the instrument. Another key feature we report is that below the *halo strahl cross over* point we generally see a distinct deficit in the core population in the anti-strahl direction. This indicates that there are fewer particles in the part of velocity space corresponding to particles returning in the direction of the Sun, compared to that expected from the Maxwellian fit. Such a cut-off in the distribution is predicted by Maksimovic et al. (2001). However, above the *halo strahl cross over* point we do not generally see such a deficit in the distribution with respect to the modelled fits.

In the future we aim to quantify the nature of these deficits with a bespoke fitting routine which can help us to better understand the role of the interplanetary electrostatic potential could play in solar wind acceleration. We also aim to examine solar wind energetics to understand mechanisms that could be at play that could lead to the growth of the non thermal populations. With the advent of Solar Orbiter, an interesting avenue for further research would be to look at alignments with Parker Solar Probe to study the same plasma parcel with this technique.

## 7. ACKNOWLEDGMENTS

We acknowledge the NASA Parker Solar Probe Mission and SWEAP team led by Justin Kasper for use of data. The authors are grateful for PSP instrument teams for producing and making the data used in this study publicly available. The SPE level 3 data are obtained from http://sweap.cfa.harvard.edu/pub/data/sci/sweap/spe/L3/spe_sf0_pad/. JBA is supported by the Science Technology and Facilities Council (STFC) ST/T506485/1.DV is supported by STFC Ernest Rutherford Fellowship ST/P003826/1. MRB is supported by a UCL Impact Studentship, joint funded by the ESA NPI contract 4000125082/18/NL/MH/ic. CJO, DV, DS and LB receive support under STFC grant ST/S000240/1. RTW is supported by STFC Consolidated Grant ST/V006320/1. JAAR is supported by ESA NPI contract 4000127929/19/NL/MH/mg and ICETEX, reference 3933061. PLW acknowledges SWEAP support under NASA PSP Phase E contract NNN06AA01C. This work was discussed at the "Joint Electron Project" at MSSL

## REFERENCES

Anderson, B. R., Skoug, R. M., Steinberg, J. T., & McComas, D. J. 2012, Journal of Geophysical Research: Space Physics, 117

Arthur, D. 2007, Proceedings of the eighteenth annual ACM-SIAM symposium on Discrete algorithms, 1027

Bakrania, M. R., Rae, I. J., Walsh, A. P., et al. 2020, A&A, 639, A46

Berčič, L., Larson, D., Whittlesey, P., et al. 2020, The Astrophysical Journal, 892, 88

Case, A. W., Kasper, J. C., Stevens, M. L., et al. 2020, ApJS, 246, 43

Feldman, W., Asbridge, J., Bame, S., Montgomery, M., & Gary, S. 1975, Journal of Geophysical Research, 80

Gosling, J. T., Baker, D. N., Bame, S. J., et al. 1987, Journal of Geophysical Research: Space Physics, 92, 8519

Graham, G. A., Rae, I. J., Owen, C. J., et al. 2017, Journal of Geophysical Research: Space Physics, 122, 3858

Halekas, J. S., Whittlesey, P., Larson, D. E., et al. 2020, The Astrophysical Journal Supplement Series, 246, 22

Hammond, C. M., Feldman, W. C., McComas, D. J., Phillips, J. L., & Forsyth, R. J. 1996, A&A, 316, 350

Horaites, K., Boldyrev, S., Wilson, Lynn B., I., Viñas, A. F., & Merka, J. 2017, Monthly Notices of the Royal Astronomical Society, 474, 115

Jeong, S.-Y., Verscharen, D., Vocks, C., et al. 2022, The Astrophysical Journal, 927, 162

Jockers, K. 1970, A&A, 6, 219

Kasper, J. C., Abiad, R., Austin, G., et al. 2016, SSRv, 204, 131
Lemaire, J. & Scherer, M. 1971, J. Geophys. Res., 76, 7479
Levenberg, K. 1944, Quarterly of Applied Mathematics, 2, 164
Lie-Svendsen, Ø., Hansteen, V. H., & Leer, E. 1997, Journal of Geophysical Research: Space Physics, 102, 4701
Maksimovic, M., Pierrard, V., & Lemaire, J. 2001, Astrophysics and Space Science, 277, 181
Maksimovic, M., Pierrard, V., & Lemaire, J. F. 1997, A&A, 324, 725
Maksimovic, M., Zouganelis, I., Chaufray, J.-Y., et al. 2005, Journal of Geophysical Research, v.110 (2005), 110
Marsch, E. 2006, Living Reviews in Solar Physics, 3, 1
Nicolaou, G., Wicks, R., Livadiotis, G., et al. 2020, Entropy, 22
Owens, M. J., Crooker, N. U., & Schwadron, N. A. 2008, Journal of Geophysical Research: Space Physics, 113
Pedregosa, F., Varoquaux, G., Gramfort, A., et al. 2011, Journal of Machine Learning Research, 12, 2825
Rosenbauer, H., Schwenn, R., Marsch, E., et al. 1977, Journal of Geophysics Zeitschrift Geophysik, 42, 561
Saito, S. & Gary, S. P. 2007, Journal of Geophysical Research: Space Physics, 112
Scudder, J. D. & Olbert, S. 1979, Journal of Geophysical Research: Space Physics, 84, 6603
Stansby, D., Salem, C., Matteini, L., & Horbury, T. 2018, Solar Physics, 293, 155
Vocks, C., Salem, C., Lin, R. P., & Mann, G. 2005, ApJ, 627, 540
Whittlesey, P. L., Larson, D. E., Kasper, J. C., et al. 2020, The Astrophysical Journal Supplement Series, 246, 74
Woodham, L. D., Horbury, T. S., Matteini, L., et al. 2020, Astronomy & Astrophysics
Zouganelis, I., Maksimovic, M., Meyer-Vernet, N., Lamy, H., & Issautier, K. 2004, ApJ, 606, 542
Štverák, Š., Maksimovic, M., Trávníček, P. M., et al. 2009, Journal of Geophysical Research: Space Physics, 114